

Analysis of different propagation models for the estimation of the topside ionosphere and plasmasphere with an Ensemble Kalman Filter

Tatjana Gerzen¹, David Minkwitz², Michael Schmidt¹, Eren Erdogan¹

¹ Technical University Munich (TUM), Deutsches Geodätisches Forschungsinstitut (DGFI), Arcisstr. 21, Munich, Germany

² Airbus Defence and Space, Robert-Koch-Str. 1, Taufkirchen, Germany

Correspondence to: Tatjana Gerzen (tatjana.gerzen@tum.de)

Abstract.

The accuracy and availability of satellite-based applications like GNSS positioning and remote sensing crucially depend on the knowledge of the ionospheric electron density distribution. The tomography of the ionosphere is one of the major tools to provide link specific ionospheric corrections as well as to study and monitor physical processes in the ionosphere and plasmasphere. In this work, we apply an Ensemble Kalman Filter (EnKF) approach for the 4D electron density reconstruction of the topside ionosphere and plasmasphere with the focus on the investigation of different propagation models and compare them with the iterative reconstruction technique SMART+. The STEC measurements of eleven LEO satellites are assimilated into the reconstructions. We conduct a case study on a global grid with altitudes between 430 and 20200 km, for two periods of the year 2015 covering quiet to perturbed ionospheric conditions. Particularly, the performance of the methods to estimate independent STEC and electron density measurements from the three Swarm satellites is analysed. The results indicate that the methods EnKF with Exponential decay as the propagation model and SMART+ perform best, providing in summary the lowest residuals.

1 Introduction

The ionosphere is the charged part of the upper atmosphere extending from about 50 - 1000 km and going over in the plasmasphere. The characteristic property of the ionosphere is that it contains sufficient free electrons to affect the propagation of trans-ionospheric radio signals, as from telecommunication, navigation or remote sensing satellites, by refraction, diffraction and scattering. Therefore, the knowledge of the three-dimensional electron density distribution and its dynamics are of practical importance. Around 50% of the signal delays or range errors of L-band signals used in GNSS originate from altitudes above the ionospheric F2 layer, consisting of topside ionosphere and plasmasphere (cf. Klimentko et al., 2015; Chen and Yao, 2015). So far, especially the topside ionosphere and plasmasphere is not well described.

The choice of the ionospheric correction model has an essential impact on the accuracy of the estimated ionospheric delay and its uncertainty. A widely used approach for ionospheric modelling is the single-layer model, whereby the ionosphere is projected onto a two-dimensional (2D) spherical layer, typically located between 350 and 450 km. However, usually 2D models are not accurate enough to support high accuracy navigation and positioning techniques in real time (cf. e.g. Odijk 2002; Banville 2014). More accurate and precise positioning is achievable by considering the ionosphere as 3D medium. There are several activities in the ionosphere community aiming to describe the mean ionospheric behavior by the development of 3D electron density models based on

38 long-term historical data. Two widely used models are the International Reference Ionosphere model (IRI, cf.
39 Bilitza et al., 2011) and the NeQuick model (cf. Nava et al., 2008).

40 Since those models represent a mean behavior, it is essential to update them by the assimilation of actual
41 ionospheric measurements. There is a variety of approaches developed and validated for the ionospheric
42 reconstruction by the combination of actual observations with an empirical or a physical background model.
43 Hernandez-Pajares et al. (1999) present one of the first GNSS-based data-driven tomographic models, which
44 considers the ionosphere as a grid of three-dimensional voxels and the electron density within each voxel is
45 computed as a random walk time series. The voxel-based discretisation of the ionosphere is further used for
46 instance in Heise et al., 2002; Wen et al., 2007; Gerzen and Minkwitz, 2016; Gerzen et al., 2017; Wen et al., 2020.
47 These authors reconstruct the 3D ionosphere by algebraic iterative methods. An alternative is to estimate the
48 electron density as a linear combination of smooth and continuous basis functions, like e.g. spherical harmonics
49 (SPH) (Schaer 1999), B-splines (Schmidt et al., 2008; Zeilhofer, 2008; Zeilhofer et al., 2009; Olivares-Pulido et
50 al., 2019), B-splines and trigonometric B-splines (Schmidt et al. 2015), B-splines and Chapman functions (Liang
51 et al., 2015 and 2016), and empirical orthogonal functions and spherical harmonics (Howe et al., 1998).

52 Besides the algebraic methods, also techniques taking benefit of information on spatial and temporal covariance
53 information, such as Optimal Interpolation, Kalman Filter, three- and four-dimensional variational techniques and
54 Kriging, are applied to update the modelled electron density distributions (cf. Howe et al., 1998; Angling et al.,
55 2008; Minkwitz et al., 2015 and 2016; Nikoukar et al., 2015; Olivares-Pulido et al., 2019).

56 Moreover, there are approaches based on physical models, which combine the estimation of the electron density
57 with physical related variables such as neutral winds or the oxygen/nitrogen ratio (cf. Wang, et al. 2004; Scherliess
58 et al., 2009; Lee et al., 2012; Lomidze et al., 2015; Schunk, et al., 2004 and 2016; Elvidge and Angling, 2019).

59 In general, the majority of data, available for the reconstruction of the ionosphere and plasmasphere, are Slant
60 Total Electron Content (STEC) measurements, i.e. the integral of the electron density along the line of sight
61 between the GNSS satellite and receiver. Often, STEC measurements provide limited vertical information and
62 hence the modelling of the vertical the electron density distribution is hampered (cf. e.g. Dettmering, 2003). The
63 estimation of the topside ionosphere and plasmasphere poses a particular difficulty since direct electron density
64 measurements are rare and since low plasma densities at these high altitudes contribute only marginally to the
65 STEC measurements. Especially, ground-based STEC measurements are dominated by electron densities within
66 and below the characteristic F2 layer peak. Consequently, information about the plasmasphere is difficult to extract
67 from ground-based STEC measurements (cf. e.g. Spencer and Mitchell, 2011). Thus, in the presented work, we
68 concentrate on the modeling of the topside part of the ionosphere and plasmasphere and utilize only the space-
69 based STEC measurements.

70 In this paper, we introduce an Ensemble Kalman Filter to estimate the topside ionosphere and plasmasphere based
71 on space-based STEC measurements. The propagation of the analysed state vector to the next time step within a
72 Kalman Filter is a key challenge. The majority of the approaches, working with EnKF variants, uses physic-based
73 models for the propagation step (cf. e.g. Elvidge and Angling 2019; Codrescu et al., 2018; Lee et al., 2012). In
74 our work, we investigate the question how the propagation step can be realized, if a physical model is not available
75 or if the usage of a physical model is rejected as computationally time consuming. We discretize the ionosphere
76 and the plasmasphere below the GNSS orbit height by 3D voxels, initialize them with electron densities calculated
77 by the NeQuick model and update them with respect to the data. We present different methods how to perform the
78 propagation step and assess their suitability for the estimation of electron density. For this purpose, a case study

79 over quiet and perturbed ionospheric conditions in 2015 is conducted, investigating the capability of the estimates
80 to reproduce assimilated STEC as well as to reconstruct independent STEC and electron density measurements.
81 We organize the paper as follows: Section 2 describes the EnKF with the different propagation methods and the
82 generation of the initial ensembles by the NeQuick model. Section 3 outlines the validation scenario with the
83 applied data sets. Section 4 presents the obtained results. Finally, we conclude our work in Section 5 and provide
84 an outlook on the next steps.

85 **2 Estimation of the topside ionosphere and plasmasphere**

86 **2.1 Formulation of the underlying inverse problem**

87 The information about the STEC, along the satellite-to-receiver ray path s can be obtained from multi-frequency
88 GNSS measurements. In detail, STEC is a function of the electron density Ne along the ray path s , given by

$$89 \quad STEC_s = \int Ne(h, \lambda, \varphi) ds, \quad (1)$$

90 where $Ne(h, \lambda, \varphi)$ is the unknown function describing the electron density values depending on altitude h ,
91 geographic longitude λ and latitude φ .

92 The discretization of the ionosphere by a 3D grid and the assumption of a constant electron density function within
93 a fixed voxel allows the transformation of Eq. (1) into a linear system of equations

$$94 \quad STEC_s \approx \sum_{i=1}^K Ne_i \cdot h_{si} \Rightarrow y = Hx + r, \quad (2)$$

95 where y is the $(m \times 1)$ vector of the STEC measurements, x is the vector of unknown electron densities with
96 $x_i = Ne_i$ equals the electron density in the voxel i , h_{si} is the length of the ray path s in the voxel i and r is the
97 vector of measurement errors assumed to be Gaussian distributed $r \sim N(0, R)$ with expectation 0 and covariance
98 matrix R .

99 **2.2 Background model**

100 As regularisation of the inverse problem in Eq. (2), a background model often provides the initial guess of the
101 state vector x . In this study, we apply the NeQuick model version 2.0.2. The NeQuick model was developed at the
102 International Centre for Theoretical Physics (ICTP) in Trieste/Italy and at the University of Graz/Austria (cf.
103 Hochegger et al., 2000; Radicella and Leitinger, 2001; Nava et al., 2008). The daily solar flux index F10.7 is used
104 to drive the NeQuick model.

105 **2.3 Analysis step of the EnKF**

106 We apply EnKF to solve the inverse problem defined in Section 2.1. Evensen (1994) introduces the EnKF as an
107 alternative to the standard Kalman Filter (KF) in order to cope with the non-linear propagation dynamics and the
108 large dimension of the state vector and its covariance matrix. In an EnKF, a collection of realisations, called
109 ensembles, represent the state vector x and its distribution.

110 Let $X^f = [x_1^f, \dots, x_N^f]$ be a $(K \times N)$ matrix whose columns are the ensemble members, ideally following the a
111 priori distribution of the state vector x . Further, the observations collected in y are treated as random
112 variables. Therefore, we define an $(m \times N)$ ensemble of observations $Y = [y_1, y_2, \dots, y_N]$ with $y_i = y + \epsilon_i$ and a
113 random vector ϵ_i from the normal distribution $N(0, R)$.

112 We define the ensemble covariance matrix around the ensemble mean $E(X^f) = \frac{1}{N} \sum_{j=1}^N x_j^f$ as follows:

$$P^f = \frac{1}{N-1} \sum_{j=1}^N \left\{ \left(x_j^f - E(X^f) \right) \cdot \left(x_j^f - E(X^f) \right)^T \right\}. \quad (3)$$

113 In the analysis step of the EnKF, the a priori knowledge on the state vector x and its covariance matrix is updated
114 by

$$X^a = X^f + P^f H^T (R + H P^f H^T)^{-1} \cdot (Y - H X^f), \quad (4)$$

115 where the matrix X^a represents the a posteriori ensembles and hence the a posteriori state vector.

116 For the propagation of the analysed solution to the next time step, we test different propagation models described
117 in Section 2.4. In order to generate the initial ensembles $X^f(t_0)$ we use the NeQuick model and describe the
118 procedure in Section 2.5. Keeping in mind that we have to deal with an extremely large state vector (details are
119 presented in Section 3.1), the important advantage of the EnKF, for the present study, is that there is no need for
120 explicitly calculation of the ensemble covariance matrix (cf. Eq. (3)). Instead, to perform the analysis step in Eq.
121 (4) we follow the implementation suggested by Evensen (2003).

122 2.4 Considered models for the propagation step of the EnKF

123 In this section, we introduce different models to propagate the analysed solution to the next time step. With all of
124 them, we propagate the ensembles 20 minutes in time. Generally, these propagation models can be described as
125 $X^f(t_{n+1}) = F(X^a(t_n)) + W_F(t_{n+1}) + \Omega_F(t_{n+1})$. In the following subsections, we outline possible choices of the
126 model F , the systematic error W_F and the process noise Ω_F .

127 Note: Beyond the presented methods, in addition we had tested a propagation model based on “persistence”, i.e.
128 $X^f(t_{n+1}) = X^a(t_n) + W_{persistence}(t_{n+1}) + \Omega_{persistence}(t_{n+1})$. Already after a time period of about 24 hours, this method
129 had shown unreasonable effects in the reconstructions, like a completely misplaced equatorial crest region.

130 2.4.1 Method 1: Rotation

131 The method Rotation assumes that in geomagnetic coordinates, the ionosphere remains invariant in space while
132 Earth rotates below it (cf. Angling and Cannon, 2004). Thus, we propagate the analysed ensemble $X^a(t_n)$ from
133 time t_n to the next time step t_{n+1} by:

$$X^f(t_{n+1}) = Rot(X^a(t_n)) + W_{rot}(t_{n+1}). \quad (5)$$

134 To calculate $Rot(X^a(t_n))$ the geomagnetic longitude is changed corresponding to the evolution time $\Delta t = t_{n+1} -$
135 t_n , i.e. 5 degree of longitude per 20 minutes. W_{rot} denotes the systematic error introduced by approximation of
136 the true propagation of X^f by a simple rotation. We tested here the following estimation of W_{rot} :

$$W_{rot}(t_{n+1}) = ratio_{rot}(t_{n+1}) \cdot E \left(Rot(X^a(t_n)) \right) \cdot \epsilon_{1 \times N} \text{ with} \quad (6)$$

$$ratio_{rot}(t_{n+1}) = \frac{\left(x^b(t_{n+1}) - Rot(x^b(t_n)) \right)}{3 \cdot Rot(x^b(t_n))}, \quad (7)$$

137 where x^b is the electron density vector calculated by the NeQuick model and $\epsilon_{1 \times N}$ is an $(1 \times N)$ matrix of ones.
138 The division in the second equation is element-wise. The ratio $ratio_{rot}(t_{n+1})$ in Eq. (7) represents the relative

139 error introduced by the application of $Rot(x^b(t_n))$ instead of $x^b(t_{n+1})$. In this way, we obtain in Eq. (6) an
 140 approximation of the mean error introduced by approximation of the true state at time t_{n+1} by the rotation of the
 141 true state at time t_n . The factor $\frac{1}{3}$ has been chosen empirically as the result of an internal validation not presented
 142 within this paper.

143 2.4.2 Method 2: Exponential decay

144 Here we assume the electron density differences between the voxels of the analysis and the background model to
 145 be a first order Gauss-Markov sequence. These differences are propagated in time by an exponential decay function
 146 (cf. Nikoukar et al. 2015, Bust and Mitchell, 2008; Gerzen et al., 2015)

$$X^f(t_{n+1}) = X^b(t_{n+1}) \cdot \epsilon_{1 \times N} + f(t_{n+1}) \cdot [X^a(t_n) - X^b(t_n)], \quad (8)$$

147 where $X^b(t)$ is the ensemble of electron density vectors calculated by the NeQuick model for the time t as
 148 described in Section 2.5; $f(t_{n+1}) = \exp\left(-\frac{\Delta t}{\tau}\right)$; $\Delta t = t_{n+1} - t_n$; τ denotes the temporal correlation parameter
 149 chosen here as 3 hours.

150 Note: Similar to the method described here, we tested also the application of $Rot([X^a(t_n) - X^b(t_n)])$ instead of
 151 $[X^a(t_n) - X^b(t_n)]$ in Eq. (8). The results were similar and are therefore not presented here.

152 2.4.3 Method 3: Rotation with exponential decay

153 For the third method, we define the propagation model as a combination of the propagation models described in
 154 the previous subsections, in particular

$$X^f(t_{n+1}) = x^b(t_{n+1}) \cdot \epsilon_{1 \times N} + f(t_{n+1}) \cdot Rot([X^a(t_n) - x^b(t_n) \cdot \epsilon_{1 \times N}]) + W(t_{n+1}) + \sqrt{\frac{\Delta t}{20}} \cdot \Omega_{exp}(t_{n+1}). \quad (9)$$

155 The systematic error W is estimated as

$$W(t_{n+1}) = f(t_{n+1}) \cdot \frac{8}{10} \cdot W_{rot}(t_{n+1}). \quad (10)$$

156 Thereby f and W_{rot} are defined as in the two previous sections. The factor $\frac{8}{10}$ thereby is again chosen empirically.

157 The process noise Ω_{exp} is assumed to be white with $\Omega_{exp}(t_{n+1}) = f(t_{n+1}) \cdot \Omega_{rot}(t_{n+1}) + (1 - f(t_{n+1})) \cdot$
 158 $Q_{exp}(t_{n+1})$. Here the matrix Ω_{rot} consists of random realizations of the distribution $N(0, \Sigma^{rot})$ with

$$\Sigma_{ii}^{rot}(t_{n+1}) = \left(ratio_i \cdot \left\{ E \left(Rot(X^a(t_n)) \right) \right\}_i \right)^2, \quad (11)$$

159 where $ratio_i$ increases continuously depending on the altitude of the voxel i from $\frac{0.5}{100}$ for lower altitudes to $\frac{1}{100}$ for
 160 the higher altitudes (chosen empirically); $E \left(Rot(X^a(t_n)) \right)$ denotes the ensemble mean vector. The equations (9)
 161 and (11) can be interpreted as follows: For the chosen time step of 20 minutes, the standard deviation of the time
 162 model error regarding the voxel i is equal to $\sqrt{\Sigma_{ii}^{rot}(t_{n+1})} = ratio_i \cdot \left\{ E \left(Rot(X^a(t_n)) \right) \right\}_i$, varying between 0.5%
 163 and 1% of the corresponding analysed electron density in the voxel i . In detail, we generate at each time step a
 164 new vector $\rho_i \sim N(0,1)$ with $\dim(\rho_i) = 100 \times 1$ and calculate the i -th row ω_i^{rot} of Ω_{rot} by Eq. **Fehler!**
 165 **Verweisquelle konnte nicht gefunden werden..**

$$\omega_i^{rot}(t_{n+1}) = \sqrt{\Sigma_{ii}(\Omega_{rot}(t_{n+1}))} \cdot \rho_i(t_{n+1})^T. \quad (12)$$

166 The matrix $Q_{exp}(t_{n+1})$ consists of random realizations (different for each time step) consistent with the a priori
 167 covariance matrix L of the errors of the background $x^b(t_{n+1})$ (cf. Howe and Runciman, 1998). In detail: The a
 168 priori covariance is assumed to be diagonal and L_{ii} equals the square of 1% of the corresponding background
 169 model value. Then the i -th row of Q_{exp} is calculated by Eq. (13):

$$q_i(t_{n+1}) = \sqrt{L_{ii}(t_{n+1})} \cdot \rho_i(t_{n+1})^T. \quad (13)$$

170 2.5 Generation of the ensembles

171 In order to generate the ensembles we vary the F10.7 input parameter of the NeQuick model (cf. Section 2.2).
 172 First, we analysed the sensitivity of the NeQuick model on F10.7. Based on the results, we calculate a vector
 173 $\mathbf{F10.7}(t)$ of the solar radio flux index with $\dim(\mathbf{F10.7}(t)) = 100 \times 1$ and $\mathbf{F10.7}(t) \sim N\left(\mathbf{F10.7}(t), \frac{3}{100} \cdot\right.$
 174 $\left.\mathbf{F10.7}(t)\right)$ at time t . The vector $\mathbf{F10.7}$ serves as input for the NeQuick model to calculate the 100 ensembles of
 175 X^b during the considered period and the initial guess of the electron densities $X^f(t_0)$.

176 An example on the variation of the generated ensembles is provided by **Figure 1**. Particularly, we show in this
 177 figure the distribution of the differences between the ensemble of electron densities $X^b(t)$ and the NeQuick model
 178 values for DOYs 041 and 076. The residuals are depicted for a selected altitude and chosen UT times, presented
 179 through different colors (cf. subfigure history). In addition, the mean, the standard deviation (STD) and the root
 180 mean square (RMS) of the residuals are presented in the subplots.

181 2.6 Provision of a benchmark by SMART+

182 In order to provide a benchmark for the described methods, we apply SMART+ as an additional reconstruction
 183 technique. SMART+ is a combination of an iterative simultaneous multiplicative column normalized method
 184 SMART (cf. Gerzen and Minkwitz, 2016) and a 3D successive correction method (3D SCM) (cf. e.g. Kalnay,
 185 2011; Gerzen and Minkwitz, 2016). As first step, SMART distributes the STEC measurements among the electron
 186 densities in the ray-path intersected voxels. For a voxel i , the multiplicative innovation is calculated as a weighted
 187 mean of the ratios between the actual measurements and the currently expected measurements. The weights are
 188 given by the length of the ray path corresponding to the measurement in the voxel i divided by the sum of lengths
 189 of all rays crossing the voxel i . Consequently, only voxels intersected by at least one measurement are innovated
 190 during the SMART procedure. Thereafter, assuming non-zero correlations between the ray path intersected voxels
 191 and those not intersected by any STEC, an extrapolation is done from intersected to not intersected voxels. For
 192 this purpose, one iteration of the 3D SCM is applied. For more details we refer to Gerzen and Minkwitz (2016)
 193 and Gerzen et al. (2017).

194 For SMART+ the number of iterations at each time step is set to 25 and the correlation coefficients are chosen as
 195 described in Gerzen and Minkwitz (2016). For each time step, SMART+ reconstructs the electron densities based
 196 on the background model (here NeQuick) and the currently available measurements. In other words, there is no
 197 propagation of the estimated electron densities from a time step t_n to the time step t_{n+1} .

198 3 Validation scenario

199 Within this study, the EnKF with the different propagation methods is applied and validated for the tomography
200 of the topside ionosphere and plasmasphere. Two periods with quiet (DOY 041-059, 2015) and perturbed (DOY
201 074-079, 2015) ionospheric conditions are analysed. In this scope, we investigate the ability to reproduce
202 assimilated STEC as well as to estimate independent STEC measurements and in-situ electron density
203 measurements of the Swarm Langmuir Probes (LP). In addition, we apply the tomography approach SMART+
204 (cf. Section 2.6) to provide a benchmark.

205 3.1 Reconstruction area

206 We estimate the electron density over the entire globe with a spatial resolution of 2.5 degrees in geodetic latitude
207 and longitude. Altitudes between 430 km and 20 200 km are reconstructed where the resolution equals 30 km for
208 altitudes from 430 km to 1000 km and decreases exponentially with increasing altitude for altitudes above 1000
209 km, i.e. in total 42 altitudes. Consequently, the number of unknowns is $K = 217728$. The temporal resolution Δt
210 is set to 20 minutes.

211 3.2 Ionospheric conditions in the considered periods

212 We use the solar radio flux F10.7, the global planetary 3h index Kp and the geomagnetic disturbance storm time
213 (DST) index to characterize the ionospheric conditions during the periods of DOY 041-059 and DOY 074-079
214 2015. In the February period (DOY 041-059, 2015) the ionosphere is evaluated as quiet with F10.7 between 108
215 and 137 sfu, a Kp index below 6 (on two days between 4 and 6, during the rest of the period below 4) and DST
216 values between 20 and -60 nT. The 17-th of March (DOY 076) 2015 is known as the St. Patrick's Day storm. The
217 F10.7 value equals ~116 sfu on DOY 075 and ~113 sfu on DOY076, the Kp index is below 5 on DOY 075 and
218 increases to 8 on DOY 076; DST drops down to -200nT on DOY 076.

219 3.3 Data

220 3.3.1 STEC measurements

221 As input for the tomography approaches and for the validation, we use space-based calibrated STEC measurements
222 of the following LEO satellite missions: COSMIC, Swarm, TerraSAR-X, MetOpA and MetOpB, and GRACE.
223 Please note that in 2015, the orbit height of the COSMIC and MetOp satellites is ~800 km, the orbit height of the
224 Swarm B and TerraSAR-X satellites is ~500 km and the one of the Swarm C satellite ~460 km. The STEC
225 measurements of Swarm A and GRACE are used for the validation only. The Swarm A satellite flew side by side
226 with the Swarm C satellite at around 460 km height. The height of the GRACE orbit was around 430 km. All
227 satellites flew at almost polar orbits. More information about the LEO satellites may be found on the following
228 webpages:

229 COSMIC: (<https://www.nasa.gov/directorates/heo/scan/services/missions/earth/COSMIC.html>),

230 Swarm: (https://www.esa.int/Applications/Observing_the_Earth/Swarm),

231 TerraSAR-X: (<https://earth.esa.int/web/eoportal/satellite-missions/t/terrasar-x>),

232 MetOpA and MetOpB: (<https://directory.eoportal.org/web/eoportal/satellite-missions/m/metop>),

233 GRACE: (https://www.nasa.gov/mission_pages/Grace/index.html).

234 The STEC measurements of the Swarm satellites are acquired from <https://swarm-diss.eo.esa.int/> and the STEC
235 measurements of the other satellite missions are downloaded from [http://cdaac-
237 www.cosmic.ucar.edu/cdaac/tar/rest.html](http://cdaac-
236 www.cosmic.ucar.edu/cdaac/tar/rest.html). Both data providers supply also information on the accuracy of the
238 STEC data. We utilize this information to fill the covariance matrix R of the measurement errors. The collected
STEC data is checked for plausibility before the assimilation.

239 3.3.2 In-situ electron density measurements from the Swarm Langmuir Probes

240 The LPs on board the Swarm satellites provide in-situ electron density measurements with a time resolution of 2
241 Hz. For the present study, the LP in-situ data are acquired from <https://swarm-diss.eo.esa.int/>. In addition, further
242 information on the pre-processing of the LP data is made available on this website.

243 Lomidze et. al (2018) assess the accuracy and reliability of the LP data (December 2013 to June 2016) by nearly
244 coincident measurements from low- and middle-latitude incoherent scatter radars, low-latitude ionosondes, and
245 COSMIC satellites, which cover all latitudes. The comparison results for each Swarm satellite are consistent across
246 these different measurement techniques. The results show that the Swarm LPs underestimate the electron density
247 systematically by about 10%.

248 4 Results

249 In this section, the different methods are presented with the following color code: blue for the method Rotation,
250 green for the method Exponential decay, light blue for the method Rotation with exponential decay, magenta for
251 NeQuick and red for SMART+. The legends in the figures are the following: “Rot” for the method Rotation, “Exp”
252 for the method Exponential decay, “Rot and Exp” for the method Rotation with exponential decay.

253 4.1 Reconstructed electron densities

254 At the end of each EnKF analysis step, we have, for each of the considered methods, 100 ensembles representing
255 the electron density values within the voxels. The EnKF reconstructed electron densities are then calculated as the
256 ensemble mean. The top subplots of **Figure 2** present the electron densities reconstructed by the method Rotation
257 with exponential decay, i.e. $E(X_{Rot\ and\ Exp}^a(t_n))$, for t_n corresponding to DOY 076, at 19:00 UT. The upper left
258 corner subplot shows horizontal layers of the topside ionosphere at different heights between 490 and 827 km. The
259 subplot in the upper right corner illustrates the plasmasphere for altitudes between 827 and 2400 km at selected
260 longitudes. The bottom line subplots show VTEC maps deduced from the 3D electron density in the considered
261 altitude range between 430 and 20200 km, where the left hand side subplot represents the reconstructed values and
262 the right hand side VTEC calculated from the NeQuick model. It is observed that the reconstructed VTEC values
263 are slightly higher than the ones of the NeQuick model.

264 **Figure 3** displays the electron density layers reconstructed by the method Rotation, i.e. $E(X_{Rot}^a(t_n))$, for t_n
265 corresponding to DOY 076, at 19:00 UT. Again, reconstructed electron densities at heights between 490 and 827
266 km (left) and the corresponding VTEC map deduced from the reconstructed 3D electron density (right) are
267 depicted. All reconstructed values seem to be plausible, showing as expected the crest region, low electron
268 densities in the Polar regions, etc. The method Rotation delivers much higher values than the NeQuick model, cf.
269 **Figure 2**. In **Figure 4**, we take a closer look at the differences between the modelled and reconstructed electron
270 densities.

271 In the following, we discuss **Figure 4 - Figure 7**, in order to understand the deviations between the reconstructions
272 produced by the different methods. On **Figure 4** the differences between the reconstructed and the modelled
273 electron densities, i.e. $E(X^a(t_n)) - x^b(t_n)$, are shown for all methods: Rotation with exponential decay, Rotation,
274 Exponential decay and SMART+ (from top left subfigure to bottom right subfigure) on DOY 076 at 19:00 UT. In
275 addition, **Figure 5** expresses these differences in percent. Please note the different ranges of the colorbars for the
276 subfigures. **Figure 6** illustrates the orbits of the LEO satellites for the STEC measurements used for the
277 reconstructions on DOY 076, at 19:00 UT (left) and the corresponding ground-track (right). The highest
278 differences are observed for the methods Rotation and Exponential decay, whereas the method Rotation with
279 exponential decay yields the smallest differences. Furthermore, as expected, the EnKF approaches provide smooth
280 and coherent patterns of differences in the ionization. Contrary, the complementary approach of SMART+ has
281 rather small patterns in areas where measurements are available and falls back to the background model in areas
282 without measurements in the surrounding. In this context, the correlation lengths between the electron densities
283 are of importance. These correlation lengths are set empirically in SMART+, whereas EnKF establishes them
284 automatically, i.e. without setting or estimating them explicitly as for instance in SMART+ or Kriging approaches.
285 For a comprehensive evaluation of the quality of the different reconstructions in the context of the used correlation
286 lengths, future analyses with further validation data and in dependence on the coincidences between the
287 measurement geometry and the geometry of the validation data set are necessary.

288 Taking into account the differences in **Figure 5**, for instance around 120°E, and the measurement geometry in
289 **Figure 6**, it is evident that the estimates of the EnKF are not only based on the current measurements but also on
290 a priori information obtained from assimilations before DOY 076, 2015, 19:00 UT. This is of course not the case
291 for SMART+.

292 In order to supplement the understanding on the differences between the propagation methods, **Figure 7** presents
293 the differences $E(X_{method}^f(t_{n+1})) - E(X_{method}^a(t_n))$ on the left column subfigures; and the percentage
294 differences $100 \cdot \frac{E(X_{method}^f(t_{n+1})) - E(X_{method}^a(t_n))}{\frac{1}{2} \cdot [E(X_{method}^f(t_{n+1})) + E(X_{method}^a(t_n))]}$ in the
295 right column for t_n corresponding to DOY 076, at 19:00 UT. Particularly, the methods (from top to bottom):
296 Rotation with exponential decay, Rotation and Exponential decay are presented. The differences for the methods
297 Rotation and Rotation with exponential decay clearly indicate the rotation of the crest region (cf. also **Figure 3**).
298 The method Rotation with exponential decay works less rigorously in the rotation than the method Rotation since
299 it is anchored by the background model and the rotation of the differences $X^a(t_n) - x^b(t_n)$ is damped by the
300 exponential decay function, see Eq. (9). Contrary to these two methods, the method Exponential decay tries to
301 propagate the difference $X^a(t_n) - X^b(t_n)$ to the next time step and adds them to the background $X^b(t_{n+1})$. Hence,
302 we observe in the lower left corner subplot of **Figure 7** a similar pattern as in the corresponding lower left corner
303 subplot of **Figure 4**.

304 Concluding, the different behaviour of the propagation methods in combination with the sparse measurement
305 geometry might serve as an explanation for the substantial differences observed in the VTEC maps shown in
306 **Figure 2** and **Figure 3**.

307 4.2 Plausibility check by comparison with assimilated STEC

308 In this Section, we check the ability of the methods to reproduce the assimilated STEC measurements. For that
 309 purpose, we calculate STEC along a ray path j , for all ray path geometries, using the estimated 3D electron
 310 densities, denoted as $STEC_j^{est}$, and compare them with the measured STEC, $STEC_j^{meas}$, used for the
 311 reconstruction. Then the mean deviation $\Delta STEC$ between the measurements $STEC_j^{meas}$ and the estimate $STEC_j^{est}$
 312 is calculated for each of the considered methods according to

$$\Delta STEC(t_n) = \frac{1}{m} \sum_{j=1}^m (|STEC_j^{meas}(t_n) - STEC_j^{est}(t_n)|), \quad (14)$$

313 where m = number of assimilated measurements. $\Delta STEC$ is calculated at each epoch t_n . In terms of the notation
 314 used for the Eqs. (1) - (4), we can reformulate the above formula for the mean deviation as

$$\Delta STEC(t_n) = \frac{1}{m} \sum_{j=1}^m (|y_j(t_n) - E(X_a(t_n))^T \cdot H_j|), \text{ with } H_j = j\text{-th row of } H. \quad (15)$$

315 Further, we consider the **RMS** of the deviations, in detail

$$RMS(t_n) = \sqrt{\frac{1}{m} \sum_{j=1}^m (|STEC_j^{meas}(t_n) - STEC_j^{est}(t_n)|)^2}. \quad (16)$$

316 To calculate $\Delta STEC$ and **RMS**, the same measurements are used as for the reconstruction. In this sense, the results
 317 presented in **Figure 8 - Figure 12** serves as a plausibility check, testing the ability of the methods to reproduce
 318 the assimilated TEC.

319 **Figure 8** depicts the distribution of the residuals, left subfigure for the quiet period, right subfigure for the
 320 perturbed period. The corresponding residual median, standard deviation (STD) and root mean square (RMS)
 321 values are also presented in the figure. It is worth to mention here that during the quiet period, the measured STEC
 322 is below 150 TECU. For all DOYs of the perturbed period, except DOY 076, the measured STEC is below ~130
 323 TECU. On DOY 076, the STEC values rise up to 370 TECU.

324 The NeQuick model seems to underestimate the measured topside ionosphere and plasmasphere STEC during both
 325 periods. During both periods, SMART+ seems to perform best, followed by the method Rotation. However,
 326 Rotation produces higher STD and RMS values. Compared to the NeQuick residuals, SMART+ is able to reduce
 327 the median of the residuals by up to 86% during the perturbed and up to 79% during the quiet period. The RMS is
 328 reduced by up to 48% and the STD by up to 41%. Rotation reduces the NeQuick median by up to 83%, the RMS
 329 by up to 27%, the STD value is almost on the same level as for NeQuick. The method Exponential decay is able
 330 to decrease the median of the NeQuick residuals by up to 54%, the RMS by up to 25%, and the STD values by up
 331 to 13%. The method Rotation with exponential decay performs similar to the NeQuick model. The latter could
 332 indicate that the parameters chosen for the error terms and weighting in Eq. (9) could still be improved, although
 333 an extensive validation of these parameters was performed prior to the analyses presented in this paper and the
 334 best configuration was selected.

335 Interestingly, the median values are higher during the quiet period, while the STD values are on the same level
 336 compared between perturbed and quiet periods. The reason therefore is probably that the assimilated STEC values
 337 have in average lower magnitude during the days in the perturbed period, compared to those during the quiet period

338 (which explains the lower median), except the storm DOY 076, while on DOY 076 they are significantly higher
339 (which explains the comparable STD).

340 **Figure 9** and **Figure 10** plot $\Delta STEC$ values versus time for the selected periods. Noticeable is the increase of
341 $\Delta STEC$ during the storm on DOY 76. On the rest of the period, $\Delta STEC$ is below eight TECU. During both periods,
342 SMART+ generates the lowest $\Delta STEC$ values. $\Delta STEC$ of the methods Rotation and Exponential decay are in most
343 of the cases higher than SMART+ delta STEC values and lower than the NeQuick model. $\Delta STEC$ of the method
344 Rotation with exponential decay is similar to the NeQuick model.

345 **Figure 11** and **Figure 12** present the distribution of $\Delta STEC$ and the *RMS* error (cf. Eq. (15)) for the quiet and
346 perturbed periods respectively. **Figure 11** confirms the conclusions we draw so far from **Figure 8** and **Figure 9** .
347 SMART+ delivers the lowest $\Delta STEC$ and *RMS* values, followed by the method Rotation and then by the method
348 Exponential decay. Rotation with exponential decay performs similar to the NeQuick model. For the perturbed
349 period, again SMART+ delivers the lowest $\Delta STEC$ and *RMS* statistics, followed by the Exponential decay and
350 the Rotation with similar results.

351 4.3 Validation with independent space-based sTEC data

352 In order to validate the methods with respect to their capability to estimate independent STEC, the LEO satellites
353 Swarm A and GRACE have been used. The STEC measurements of these satellites are not assimilated by the
354 tested methods.

355 For each of the three LEOs, the residuals between $STEC^{meas}$ and $STEC^{est}$ are calculated and denoted as $dTEC =$
356 $STEC^{meas} - STEC^{est}$. Further, the absolute values of the residuals $|dTEC|$ are considered.

357 In general, for the quiet period, the STEC measurements of Swarm A vary below 105 TECU and for the second
358 period below 170 TECU. For the GRACE satellite, the STEC measurements are below 282 TECU for the quiet
359 period and below 264 TECU for the second period.

360 **Figure 13** and **Figure 14** display the histograms of the STEC residuals during the quiet period for Swarm A and
361 GRACE respectively. Presented are the distributions of the residuals $dTEC$ and the absolute residuals $|dTEC|$.
362 Also plotted are the median, STD and RMS of the corresponding residuals. **Figure 15** and **Figure 16** depict the
363 histograms of the STEC residuals during the perturbed period.

364 Again, the NeQuick model seems to underestimate the measured STEC during both periods for GRACE and
365 Swarm A satellites. Compared to the NeQuick model, during both periods, the methods SMART+ and Exponential
366 decay decrease the residuals and the absolute residuals between measured and estimated STEC for both GRACE
367 and Swarm A satellites. The method Rotation with exponential decay performs for both periods very similar to the
368 NeQuick model. The performance of the method Rotation is partly even worse than the one of the background
369 model. Our impression is that the number and the distribution of the assimilated measurements is too small and
370 angle limited to be sufficient to dispense with a background model, as is the case with the Rotation method, which
371 uses the model only for the estimation of the systematic error.

372 Regarding the STEC of Swarm A, the lowest residuals and the most reduction in comparison to the NeQuick
373 model, are achieved by SMART+. The median and the STD of the SMART+ residuals are ~ 0.3 TECU and ~ 3.4
374 TECU respectively for quiet and ~ 0.7 TECU and ~ 7 TECU for the perturbed period. Compared to the NeQuick
375 model, the absolute median value is reduced up to 64% by SMART+ during the quiet and by up to 61% during the

376 perturbed period. The STD value is decreased by up to 47% during the quiet and up to 29% during the storm
377 period. The second lowest residuals are achieved by the Exponential decay - here the median of the residuals is
378 around 0.2 TECU for quiet and around 0.8 TECU for the perturbed period.

379 Regarding the STEC of GRACE during the quiet period, the lowest residuals and the most reduction in comparison
380 to background, are achieved by the Exponential decay, followed by SMART+. Exponential decay reduces the
381 background absolute median value by up to 26% and the STD value by up to 28%. The median of the residuals is
382 around 0.2 TECU. For SMART+, the median of the residuals is around 2.9 TECU. During the perturbed period,
383 SMART+ reduces the absolute median at most by 17% and the STD by 9%, the Exponential decay does not reduce
384 the absolute median, compared to NeQuick, but it reduces the absolute STD value by 23%. The median of the
385 residuals are around -0.5 TECU for Exponential decay and around 0.8 TECU for SMART+.

386 Comparing between quiet and storm conditions, in general an increase of RMS and STD of the SWARM A
387 residuals is observable for the NeQuick model and all tomography methods regarding both satellites. This is not
388 the case for the GRACE residuals.

389 4.4 Validation with independent LP in-situ electron densities

390 In this section, we further extend our analyses to the validation of the methods with independent LP in-situ electron
391 densities of the three Swarm satellites. According to the locations of the LP measurements, the estimated electron
392 density values are interpolated (by a 3D interpolation, using the MATLAB build-in function
393 scatteredInterpolan.m) from the 3D electron density reconstructions. For each satellite, the measured electron
394 density Ne^{meas} is compared to the estimated one Ne^{est} . In particular we calculate the residuals $dNe = Ne^{meas} -$
395 Ne^{est} , the absolute residuals $|dNe|$, the relative residuals $dNe_{rel} = \frac{dNe}{Ne^{meas}} \cdot 100\%$ and the absolute relative
396 residuals $|dNe_{rel}|$.

397 **Figure 17** depicts the distribution of the residuals dNe for the quiet period along with the median, STD and RMS
398 values. Each of the three subplots presents one of the Swarm satellites. In **Figure 18** the histograms of $|dNe|$ and
399 $|dNe_{rel}|$ are given for the same period. In **Figure 18** we do not separate the values for the different satellites,
400 because these are similar. **Figure 19** and **Figure 20** show the corresponding histograms for the perturbed period.

401 The electron densities of the NeQuick model are in median slightly higher than the LP in-situ measurements for
402 all three satellites during both periods. The median and STD values for the $|dNe_{rel}|$ residuals produced by
403 NeQuick are $\sim 33\%$ and $\sim 38\%$ resp. during the quiet period. For the perturbed period, we observe higher median
404 and STD values of $\sim 45\%$ and $\sim 56\%$, resp. The increase of the RMS and STD values of the absolute residuals is
405 also visible for all the considered reconstruction methods.

406 The methods SMART+ and Rotation with exponential decay follow the trend of the model and show similar
407 distributions in **Figure 17** and **Figure 19**. Comparing these two methods with the NeQuick model, the performance
408 of SMART+ is slightly better reducing the median of the absolute and absolute relative residuals by up to 8%.
409 Further, during both periods, SMART+ reduces the STD values of the $|dNe|$ values by up to 23%. However, the
410 STD and RMS values of the $|dNe_{rel}|$ residuals for SMART+ during the quiet period are higher than those of the
411 NeQuick model. The median and STD values of the $|dNe_{rel}|$ residuals for SMART+ are $\sim 30\%$ and $\sim 43\%$ resp.
412 during quiet and higher during perturbed period, namely $\sim 43\%$ and $\sim 53\%$ resp. The statistics of the methods
413 Exponential decay and Rotation are worse than those of NeQuick.

414 5 Summary and conclusions

415 In this paper, we assess three different propagation methods for an Ensemble Kalman Filter approach in the case
416 that a physical propagation model is not available or discarded due to computational burden. We validate these
417 methods with independent STEC observations of the satellites GRACE and Swarm A and with independent
418 Langmuir probes data of the three Swarm satellites. The methods are compared to the algebraic reconstruction
419 method SMART+, serving as a benchmark and to the background model NeQuick for periods of the year 2015
420 covering quiet to perturbed ionospheric conditions.

421 Overlooking all the validation results, the methods SMART+ and Exponential decay reveal the best performance
422 with the lowest residuals, whereas the method Rotation with exponential decay provides only a small improvement
423 compared to the NeQuick model. While SMART+ modifies the electron densities of the background model around
424 the measurement geometry and produces rather small patches, the EnKF produces larger and smoother patterns.
425 As expected, the validations indicate that the electron density estimates of the EnKF are not only dependent on the
426 current measurement geometry but also on prior assimilations.

427 The plausibility check in section 4.2 shows that all methods reduce successfully the STEC residuals and provide
428 better results than the background model. SMART+ demonstrates the best performance and lowers the error
429 statistics of the NeQuick model by up to 86%, followed by the method Rotation, decreasing the median of the
430 residuals by up to 83%. The method Exponential decay reduces the median by up to 55%, but the STD values stay
431 almost on the same level as for the NeQuick model.

432 Although the EnKF with the method Rotation reproduces the assimilated STEC data well, less accurate estimates
433 are obtained in the validation with independent data. We assume this has two main reasons: First, as the only
434 propagation method, Rotation is not anchored by the background model. Second, the number of the assimilated
435 measurements is low compared to the number of unknowns and the available measurements are unevenly
436 distributed and angle limited. Both together could lead to increased deviations of the estimates from the truth.

437 The methods SMART+ and the EnKF with Exponential decay provide the best estimates of the independent STEC
438 and reduce the STEC residuals by up to 64% for Swarm A and 28% for GRACE, compared to the NeQuick model.
439 SMART+ generates the smallest residuals for the STEC measurements of Swarm A and Exponential decay
440 performs at best for STEC measurements of GRACE.

441 Concerning the estimation of independent electron densities of the Langmuir Probes, SMART+ shows the best
442 results, reducing the absolute residuals by up to 23%. The median and STD values of the absolute residuals
443 $|dN_{e_{rel}}|$ for SMART+ are $\sim 30\%$ and $\sim 43\%$ respectively during quiet ionospheric conditions and $\sim 43\%$ and
444 $\sim 53\%$ respectively during perturbed ionospheric conditions. The distributions of the residuals produced by
445 Rotation with exponential decay are similar to the ones of the NeQuick model. In general, all the considered
446 methods generate relatively high residuals. These observations could be explained by the fact that the independent
447 electron density measurements are located at the lower edge of the reconstructed area and all the assimilated
448 measurements are located above. Additionally, Swarm LPs was found to underestimate the true electron density
449 systematically, cf. Section 3.3.2. In order to obtain better results for the lower altitudes, it might therefore be
450 necessary to apply a kind of anchor point for the lower altitudes within the reconstruction procedure which could
451 for instance be the Swarm LPs electron density measurements themselves.

452 Another approach to improve the reconstructions could be to precondition the background model, e.g. in terms of
453 F2 layer characteristics or the plasmopause location (cf. e.g. Bidaine and Warnant, 2010, Gerzen et. al., 2017).

454 To get a comprehensive final impression of the performance of the investigated methods and to gain insight into
455 the ability of the methods to correctly characterize the shapes of the electron density profiles, we intend to continue
456 the validation of the methods with additional independent measurements of the plasmasphere and topside
457 ionosphere, e.g. coherent scatter radar data.

458 **Acknowledgements**

459 We thank the NOAA (ftp://ftp.ngdc.noaa.gov/STP/GEOMAGNETIC_DATA/INDICES/) and WDC Kyoto
460 (<http://wdc.kugi.kyoto-u.ac.jp/dstdir/index.html>) for making available the geo-related data, F10.7, Kp and DST
461 indices. We are grateful to the European Space Agency for providing the Swarm data ([https://swarm-
462 diss.eo.esa.int/](https://swarm-diss.eo.esa.int/)) and to the CDAAC: COSMIC Data Analysis and Archive Center for providing the STEC data of
463 several LEO satellites (<http://cdaac-www.cosmic.ucar.edu/cdaac/tar/rest.html>). Additionally, we express our
464 gratitude to the Aeronomy and Radiopropagation Laboratory of the Abdus Salam International Centre for
465 Theoretical Physics Trieste/Italy for providing the NeQuick version 2.0.2 for scientific purposes. This study was
466 performed as part of the MuSE project (<https://gepris.dfg.de/gepris/projekt/273481272?language=en>), funded by
467 the DFG as a part of the Priority Programme “DynamicEarth”, SPP-1788.

468 **References**

- 469 Angling, M. J.: First assimilation of COSMIC radio occultation data into the Electron Density Assimilative Model
470 (EDAM), *Ann. Geophys.*, 26, 353-359, 2008.
- 471 Angling, M. J. and Cannon, P. S.: Assimilation of radio occultation measurements into background ionospheric
472 models, *Radio Sci.*, 39, RS1S08, doi:10.1029/2002RS002819, 2004.
- 473 Banville, S.: Improved convergence for GNSS precise point positioning. Ph.D. dissertation, Department of
474 Geodesy and Geomatics Engineering, Technical Report No. 294, University of New Brunswick, Fredericton, New
475 Brunswick, Canada, 2014.
- 476 Bidaine B. and R. Warnant: Assessment of the NeQuick model at mid-latitudes using GNSS TEC and ionosonde
477 data, *Adv. Space Res.*, 45, 1122-1128, 2010.
- 478 Bilitza, D., L.-A. McKinnell, B. Reinisch, and T. Fuller-Rowell: The International Reference Ionosphere (IRI)
479 today and in the future, *J. Geodesy*, 85:909-920, DOI 10.1007/s00190-010-0427-x, 2011.
- 480 Bust, G. S., and C. N. Mitchell: History, current state, and future directions of ionospheric imaging, *Rev. Geophys.*,
481 46, RG1003, doi:10.1029/2006RG000212, 2008.
- 482 Chen P., Y. Yao: Research on global plasmaspheric electron content by using LEO occultation and GPS data, *Adv.*
483 *Space Res.*, 55, 2248–2255, doi:10.1016/j.asr.2015.02.004, 2015.
- 484 Codrescu, S. M., M. V. Codrescu, M. Fedrizzi: An Ensemble Kalman Filter for the thermosphere-ionosphere. *Space*
485 *Weather*, 16, 57–68, <https://doi.org/10.1002/2017SW001752>, 2018.
- 486 Dettmering D.: Die Nutzung des GPS zur dreidimensionalen Ionosphärenmodellierung. PhD Thesis, University of
487 Stuttgart, <http://elib.uni-stuttgart.de/opus/volltexte/2003/1411/>, 2003.
- 488 Elvidge, S., and M. J. Angling: Using the local ensemble Transform Kalman Filter for upper atmospheric
489 modelling, *J. Space Weather Space Clim.*, 9, A3, <https://doi.org/10.1051/swsc/2019018>, 2019.
- 490 Evensen, G.: Sequential data assimilation with a nonlinear quasi-geostrophic model using Monte Carlo methods
491 to forecast error statistics, *J. Geophys. Res.*, 99 (C5), 10143– 10162, doi:10.1029/94JC00572, 1994.
- 492 Evensen, G.: The Ensemble Kalman Filter: theoretical formulation and practical implementation, *Ocean Dynamics*,
493 53, 343-367, DOI 10.1007/s10236-003-0036-9, 2003.
- 494 Howe, B. M., K Runciman, J. A. Secan, Tomography of the ionosphere: Four-dimensional simulations, *Radio Sci.*,
495 33, 1, 109-128, 1998.
- 496 Gerzen, T., Minkwitz, D., and Schlueter, S.: Comparing different assimilation techniques for the ionospheric F2
497 layer reconstruction, *J. Geophys. Res.-Space*, 120, 6901–6913, doi:10.1002/2015JA021067, 2015.

498 Gerzen, T. and D. Minkwitz, Simultaneous multiplicative column normalized method (SMART) for the 3D
499 ionosphere tomography in comparison with other algebraic methods, *Ann. Geophys.*, 34, 97-115, doi:
500 10.5194/angeo-34-97-2016, 2016.

501 Gerzen, T., V. Wilken, D. Minkwitz, M. Hoque, S. Schlüter: Three-dimensional data assimilation for ionospheric
502 reference scenarios, *Ann. Geophys.*, 35, 203-215, doi:10.5194/angeo-35-203-2017, 2017.

503 Heise, S., N. Jakowski, A. Wehrenpfennig, Ch. Reigber, H. Lühr: Sounding of the topside
504 ionosphere/plasmasphere based on GPS measurements from CHAMP: Initial results, *Geophys. Res. Letters*,
505 29(14), doi: 10.1029/2002GL014738, 2002.

506 Hernandez-Pajares, M., J.M. Juan, J. Sanz: New approaches in global ionospheric determination using ground
507 GPS data. *J Atmos Solar Terr Phys*, 61: 1237-1247, 1999.

508 Hochegger G., Nava B., Radicella S.M., and R. Leitinger: A Family of Ionospheric Models for Different Uses,
509 *Phys. Chem. Earth Part C Solar Terres Planet Sci*, 25, 307-310, doi:10.1016/S1464-1917(00)00022-2, 2000.

510 Howe B., K. Runciman: Tomography of the ionosphere: Four-dimensional simulations, *Radio Sci.*, 33, 1, 09-128,
511 1998.

512 Kalnay, E.: *Atmospheric Modeling, Data Assimilation and Predictability*, Cambridge University Press,
513 Cambridge, UK, 2011.

514 Klimenko M. V., V. V. Klimenko, I. E. Zakharenkova, I. V. Cherniak: The global morphology of the
515 plasmaspheric electron content during Northern winter 2009 based on GPS/COSMIC observation and GSM TIP
516 model results. *Adv. Space Res.*, 55, 2077–2085, doi:10.1016/j.asr.2014.06.027, 2015

517 Lee, I. T., T. Matsuo, A. D. Richmond, J. Y. Liu, W. Wang, C. H. Lin, J. L. Anderson, M. Q. Chen: Assimilation
518 of FORMOSAT-3/COSMIC electron density profiles into a coupled thermosphere/ionosphere model using
519 ensemble Kalman filtering, *JGR*, 117, A10, <https://doi.org/10.1029/2012JA017700>, 2012.

520 Liang, W., M. Limberger, M. Schmidt, D. Dettmering, U. Hugentobler, D. Bilitza, N. Jakowski, M.M. Hoque, V.
521 Wilken, T. Gerzen: Regional modeling of ionospheric peak parameters using GNSS data - an update for IRI. *Adv.*
522 *Space Res.*, 55(8), 1981-1993, 10.1016/j.asr.2014.12.006, 2015.

523 Liang, W., M. Limberger, M. Schmidt, D. Dettmering, U. Hugentobler: Combination of ground- and space-based
524 GPS data for the determination of a multi-scale regional 4-D ionosphere model. In: Rizos C., Willis P. (Eds.) *IAG*
525 *150 Years, IAG Symposia*, 143, 751-758, 10.1007/1345_2015_25, 2016.

526 Lomidze, L., L. Scherliess, R. W. Schunk: Magnetic meridional winds in the thermosphere obtained from Global
527 Assimilation of Ionospheric Measurements (GAIM) model, *JGR: Space Physics*, 120, 9, 8025-8044,
528 <https://doi.org/10.1002/2015JA021098>, 2015.

529 Lomidze, L., D. J. Knudsen, J. Burchill, A. Kouznetsov, S. C. Buchert: Calibration and validation of Swarm plasma
530 densities and electron temperatures using ground-based radars and satellite radio occultation measurements, *Radio*
531 *Sci.*, 53, 15– 36, <https://doi.org/10.1002/2017RS006415>, 2018.

532 Minkwitz, D., K.G. van den Boogaart, T. Gerzen, M.M. Hoque: Tomography of the ionospheric electron density
533 with geostatistical inversion, *Ann. Geophys.*, 33, 1071–1079, <https://doi.org/10.5194/angeo-33-1071-2015>, 2015.

534 Minkwitz, D., K. G. van den Boogaart, T. Gerzen, M. Hoque, M. Hernández-Pajares: Ionospheric tomography by
535 gradient enhanced kriging with STEC measurements and ionosonde characteristics, *Ann. Geophys.*, 34, 999-1010,
536 doi:10.5194/angeo-34-999-2016, 2016.

537 Nava B., P. Coisson, and S.M. Radicella: A new version of the NeQuick ionosphere electron density model, *J.*
538 *Atmos. Sol-Terr. Phy.*, 70, 1856-1862, doi:10.1016/j.jastp.2008.01.015, 2008.

539 Nikoukar, R., G. Bust, D. Murr: Anovel data assimilation technique for the plasmasphere, *J. Geophys. Res.*,
540 *Space Physics*, 120, 8470-8485, doi:10.1002/2015JA021455, 2015.

541 Odijk, D.: Precise GPS positioning in the presence of ionospheric delays. *Publications on geodesy, Vol. 52. The*
542 *Netherlands Geodetic Commission, Delft. ISBN-13: 978 90 6132 278 8*, 2002.

543 Olivares-Pulido G., M. Terkildsen, K. Arsov, P.J.G. Teunissen, A. Khodabandeh, V. Janssen: A 4D tomographic
544 ionospheric model to support PPP-RTK, *Journal of Geodesy*, 93, 9, 1673-1683, [https://doi.org/10.1007/s00190-](https://doi.org/10.1007/s00190-019-01276-4)
545 [019-01276-4](https://doi.org/10.1007/s00190-019-01276-4), 2019.

546 Radicella S. M., and R. Leitinger: The evolution of the DGR approach to model electron density profiles, *Adv.*
547 *Space. Res.*, 27, 35-40, doi:10.1016/S0273-1177(00)00138-1, 2001.

548 Schaer, S.: Mapping and predicting the Earth's ionosphere using the global positioning system. Ph.D. dissertation,
549 Astron Institute, University of Bern, Berne, 1999.

550 Scherliess, L., D. C. Thompson, R. W. Schunk: Ionospheric dynamics and drivers obtained from a physicsbased
551 data assimilation model, *Radio Sci.*, 44, RS0A32, doi:10.1029/2008RS004068, 2009.

552 Schmidt, M., D. Bilitza, C. Shum, C. Zeilhofer: Regional 4-D modelling of the ionospheric electron density. *Adv*
553 *Space Res* 42: 782790. <https://doi.org/10.1016/j.asr.2007.02.050>, 2008.

554 Schmidt, M., D. Dettmering, F. Seitz: Using B-spline expansions for ionosphere modeling. In: Freeden W., Nashed
555 M.Z., Sonar T. (Eds.) Handbook of Geomathematics (Second Edition), 939-983, Springer, 10.1007/978-3-642-
556 54551-1_80, 2015.

557 Schunk, R. W., et al.: Global Assimilation of Ionospheric Measurements (GAIM), Radio Sci., 39, RS1S02,
558 doi:10.1029/2002RS002794, 2004.

559 Schunk, R. W., L. Scherliess, V. Eccles, L. C. Gardner, J. J. Sojka, L. Zhu, X. Pi, A. J. Mannucci, M. Butala, B.
560 D. Wilson, A. Komjathy, C. Wang, G. Rosen: Space weather forecasting with a Multimodel Ensemble Prediction
561 System (MEPS), Radio Sci., 51, 1157–1165, doi:10.1002/2015RS005888, 2016.

562 Spencer, P. S. J., C. N. Mitchell: Imaging of 3-D plasmaspheric electron density using GPS to LEO satellite
563 differential phase observations, Radio Sci., 46, RS0D04, <https://doi.org/10.1029/2010RS004565>, 2011.

564 Wang, C., G. Hajj, X. Pi, I. G. Rosen, B. Wilson: Development of the Global Assimilative Ionospheric Model,
565 Radio Sci., 39, RS1S06, doi:10.1029/2002RS002854, 2004.

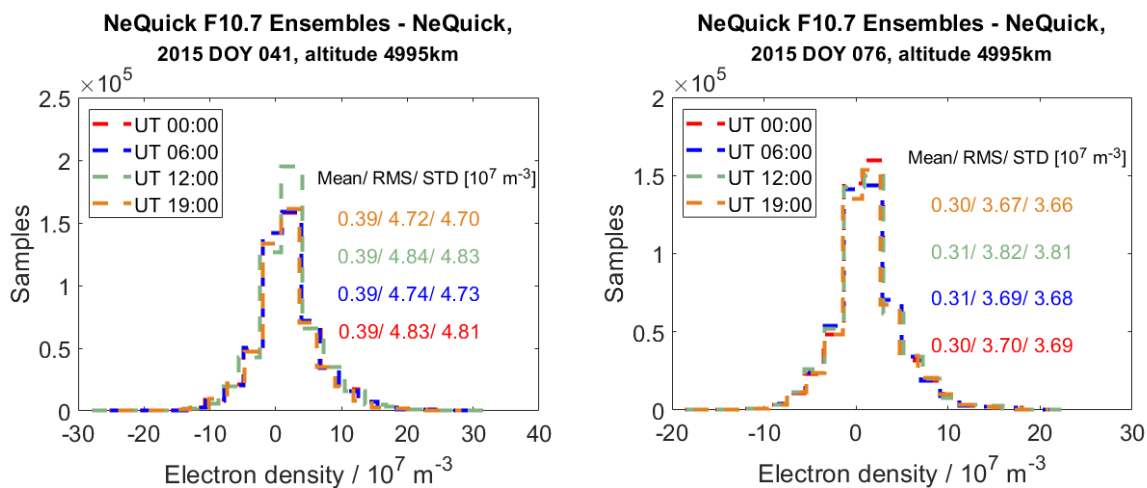
566 Wen, D., Y. Yuan, J. Ou, X. Huo, K. Zhang: Three-dimensional ionospheric tomography by an improved algebraic
567 reconstruction technique, GPS Solut., 11, 251–258, doi:10.1007/s10291-007-0055-y, 2007.

568 Wen, D., D. Mei, Y. Du: Adaptive Smoothness Constraint Ionospheric Tomography Algorithm, Sensors (Basel),
569 20, 8, doi: 10.3390/s20082404, 2020.

570 Zeilhofer, C.: Multi-dimensional B-spline Modeling of Spatio-temporal Ionospheric Signals: DGK. Series A, 123,
571 München, 2008.

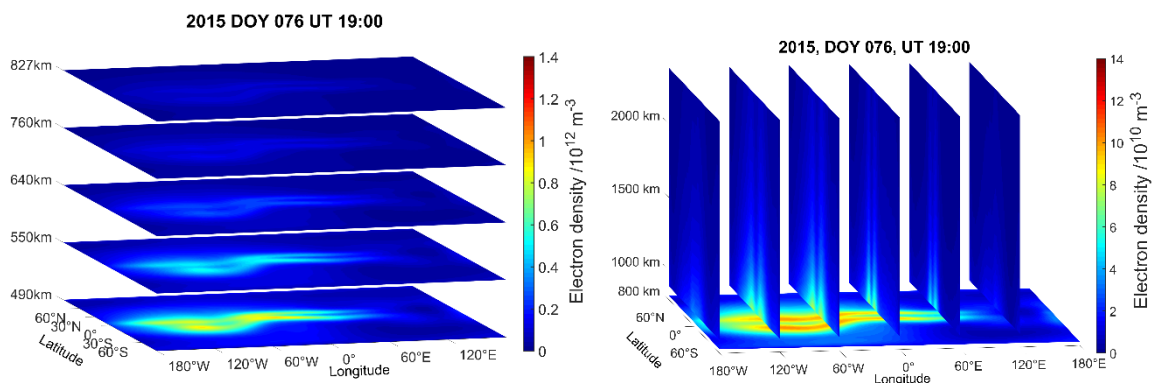
572 Zeilhofer, C., M. Schmidt, D. Bilitza, C. K. Shum: Regional 4-D modeling of the ionospheric electron density
573 from satellite data and IRI, Adv. Space Res., 43, 2009.

574



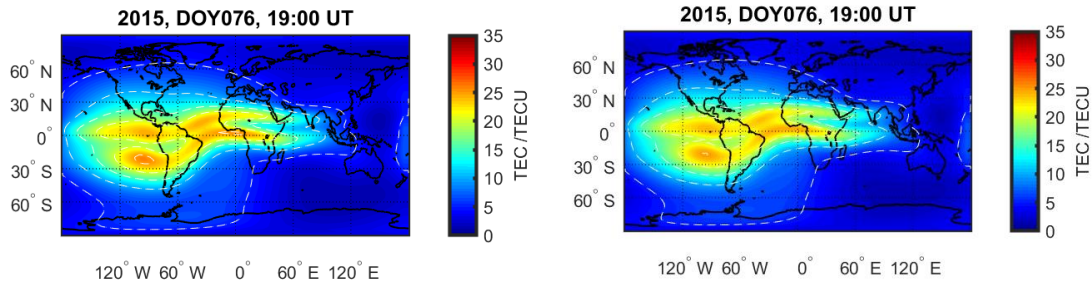
575

576 **Figure 1: The distribution of the ensemble residuals for a chosen altitude and selected UT times, for all**
577 **latitudes, longitudes. Left: for DOY 041, right: for DOY 076.**



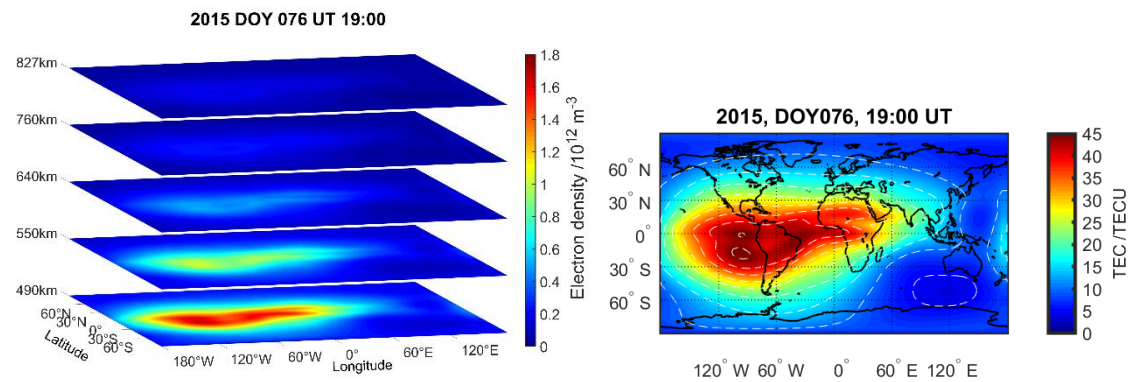
578

16



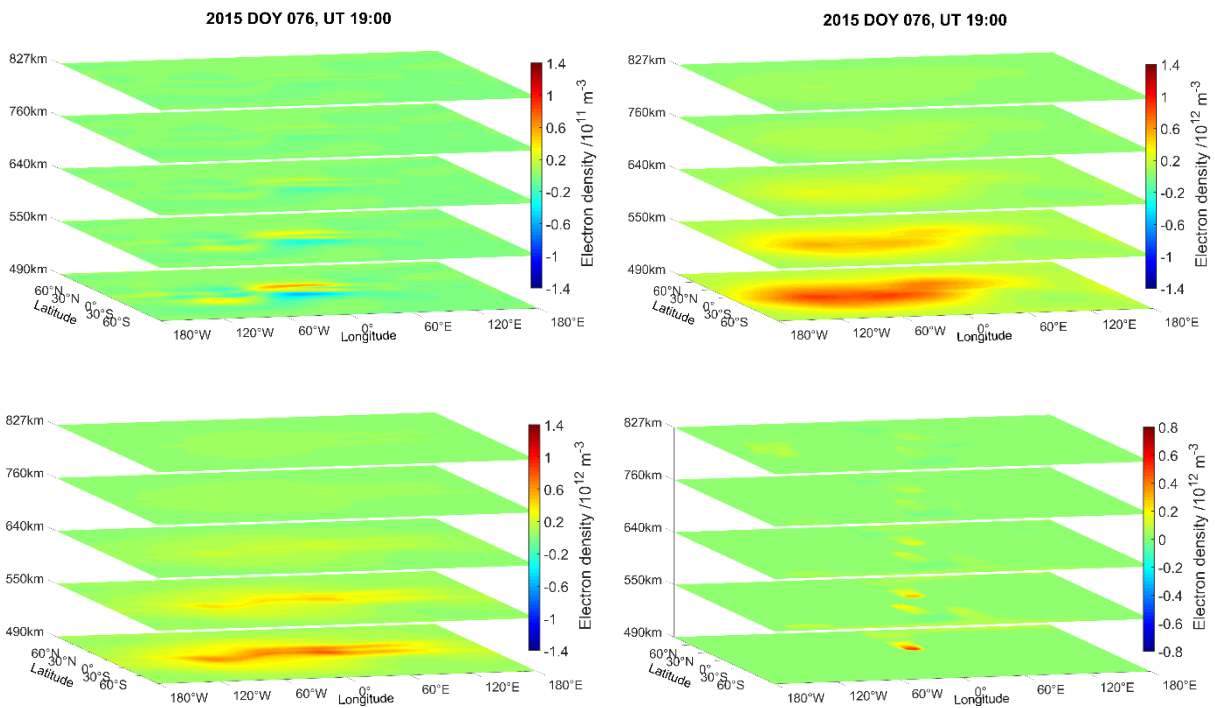
579

580 **Figure 2: Subfigures top: Rotation with exponential decay reconstructed electron density represented by**
 581 **layers at different heights between 490 and 827 km (left) and at chosen longitudes for altitudes between 827**
 582 **and 2400 km (right). Subfigures bottom: The vertical TEC map deduced from the reconstructed (left) and**
 583 **NeQuick-modeled (right) 3D electron density in the altitude range between 450 and 20200 km.**



584

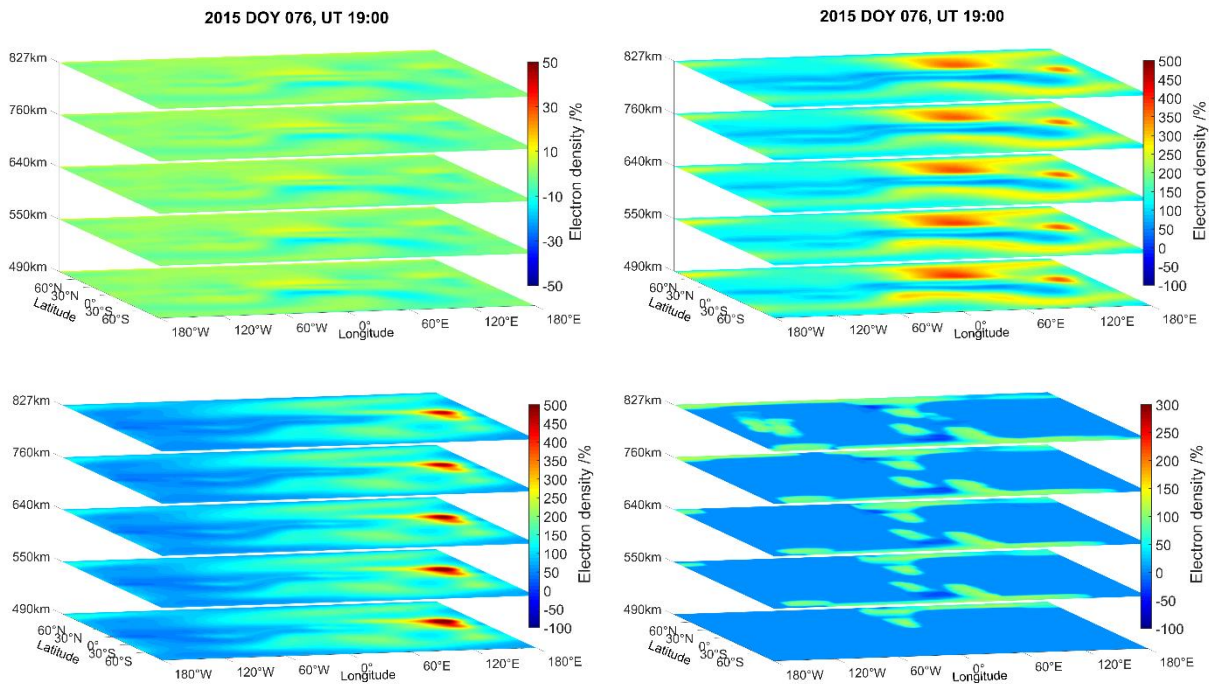
585 **Figure 3: Method Rotation reconstructed electron density represented by layers at different heights between**
 586 **490 and 827 km (left) and vertical TEC map deduced from the reconstructed 3D electron density in the**
 587 **altitude range between 450 and 20200 km (right).**



588

589

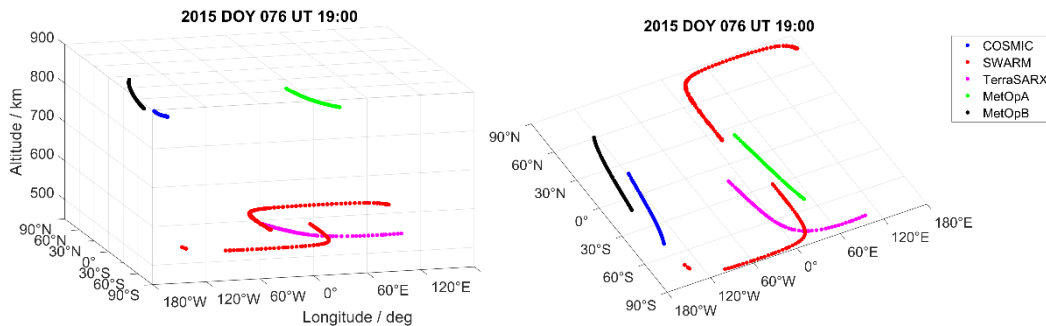
590 **Figure 4: Reconstructed minus NeQuick modeled electron density represented by layers at different heights**
 591 **between 490 and 827 km. Left top: For Rotation with exponential decay. Right top: Rotation. Left bottom:**
 592 **Exponential decay. Right bottom: SMART+.**



593

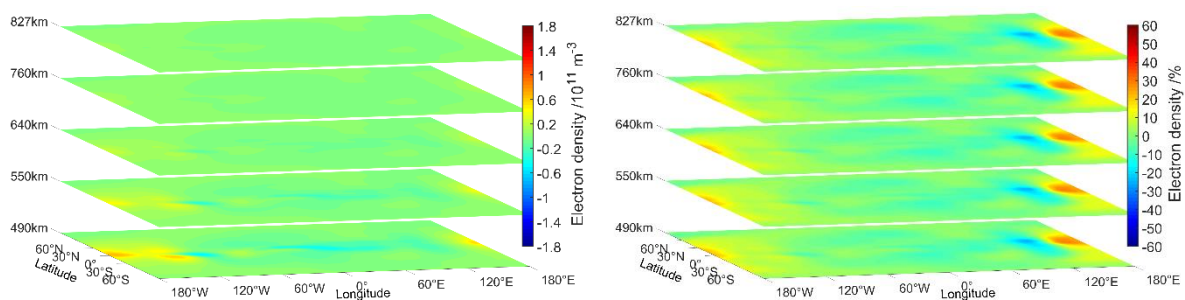
594

595 **Figure 5: Differences between reconstructed and NeQuick modeled electron density in percent, represented**
 596 **by layers at different heights between 490 and 827 km. Left top: For Rotation with exponential decay. Right**
 597 **top: Rotation. Left bottom: Exponential decay. Right bottom: SMART+.**

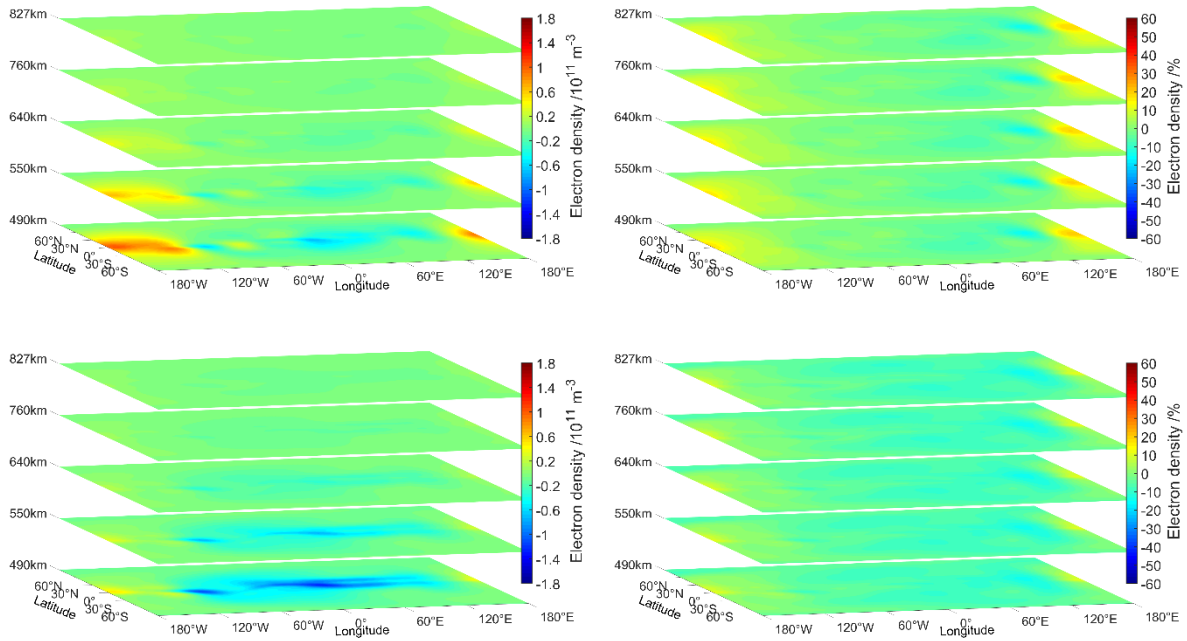


598

599 **Figure 6: The locations of the LEO satellites of the STEC measurements used for the reconstruction.**



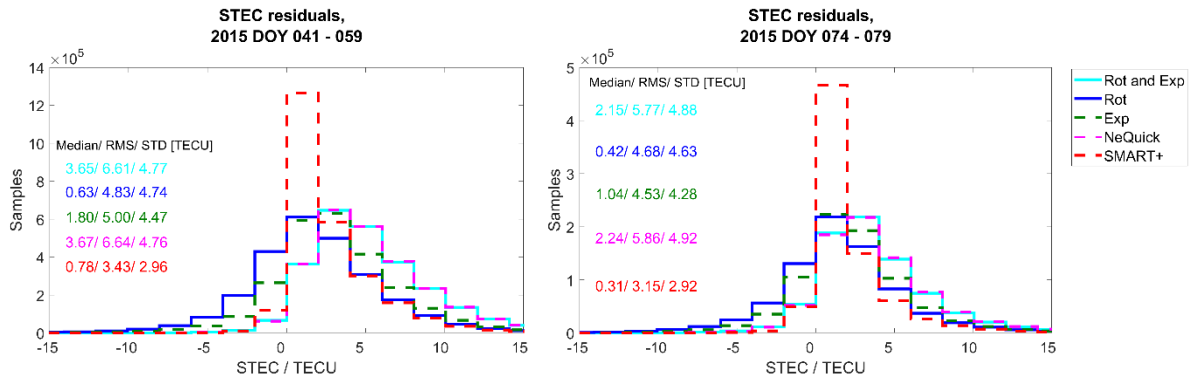
600



601

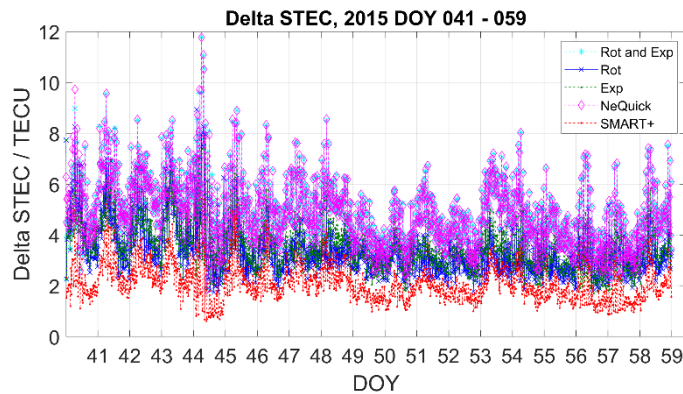
602

603 **Figure 7: Left: Differences between the forecasted and analysed electron densities, represented by layers at**
 604 **different heights between 490 and 827 km. Right: Differences in percent. Top: Method Rotation with**
 605 **exponential decay. Middle: Rotation. Bottom: Exponential decay.**



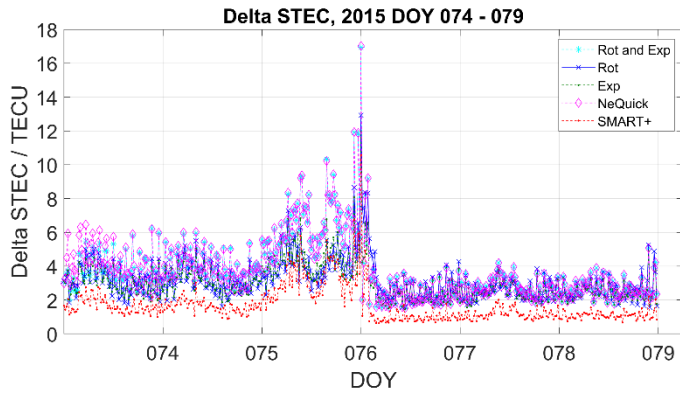
606

607 **Figure 8: Plausibility check – distributions of the STEC measured minus STEC estimated residuals. Left**
 608 **subfigure depicts residuals of the quiet period, right subfigure for the perturbed period.**



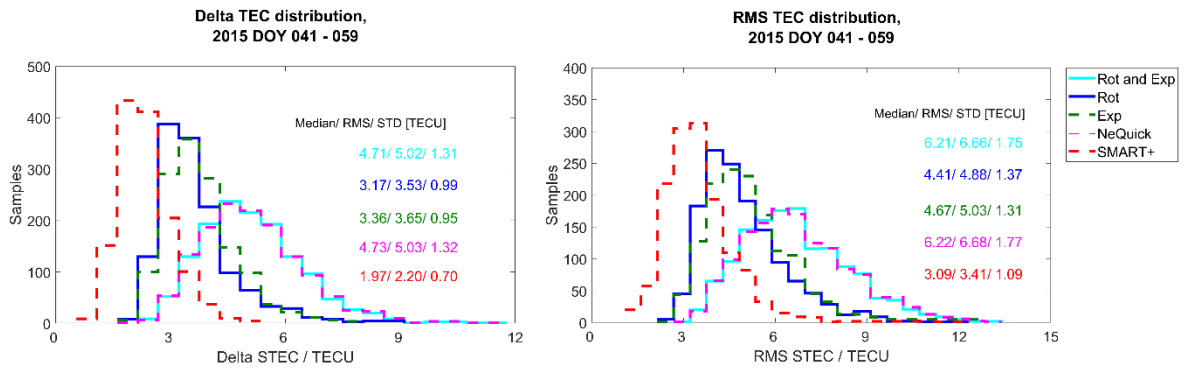
609

610 **Figure 9: Plausibility check for the quiet period – Δ STEC values versus time.**



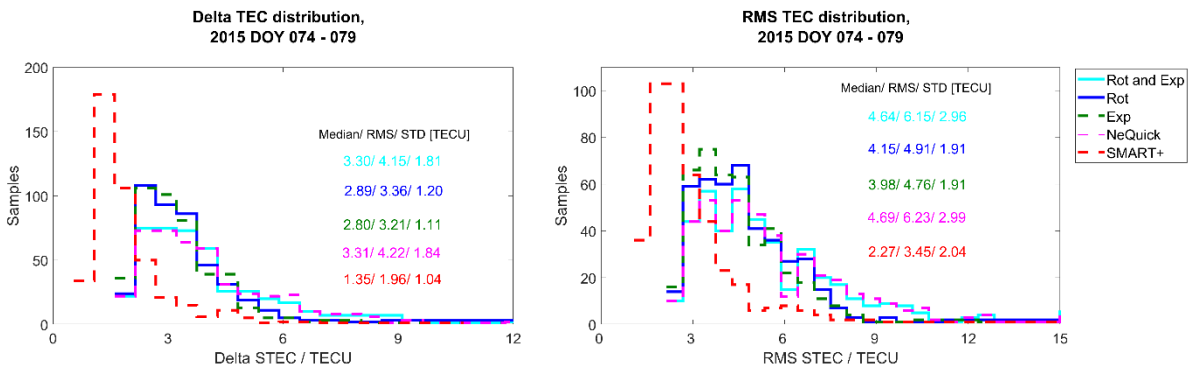
611

612 **Figure 10: Plausibility check for the perturbed period – $\Delta STEC$ values versus time.**



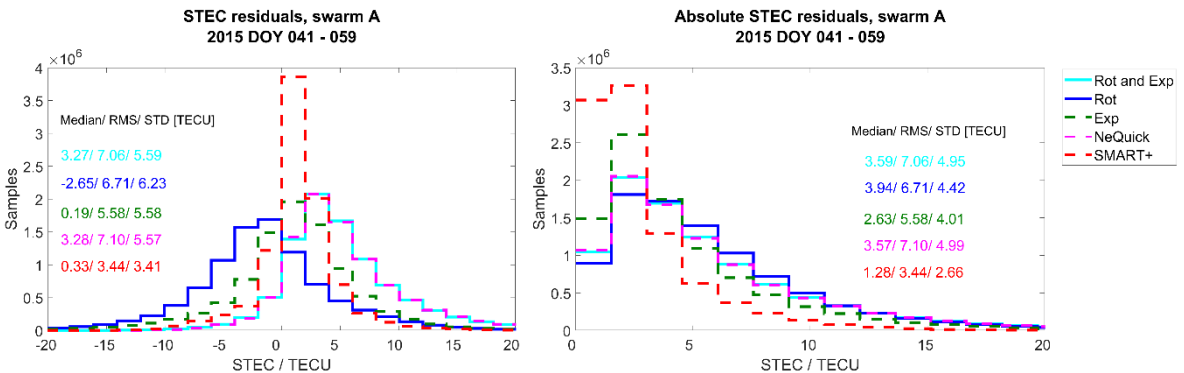
613

614 **Figure 11: Plausibility check for the quiet period – distributions of the delta TEC (left) and RMS (right)**
 615 **values.**



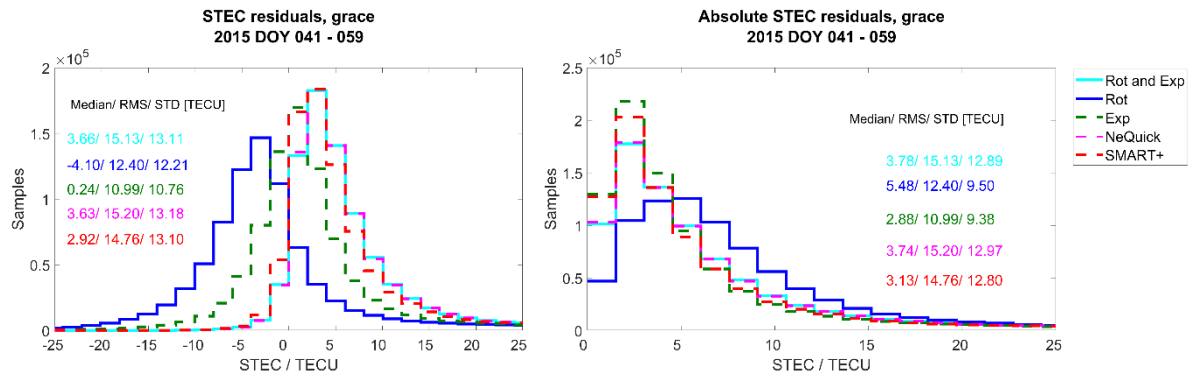
616

617 **Figure 12: Plausibility check for the perturbed period – distributions of the delta TEC (left) and RMS (right)**
 618 **values.**

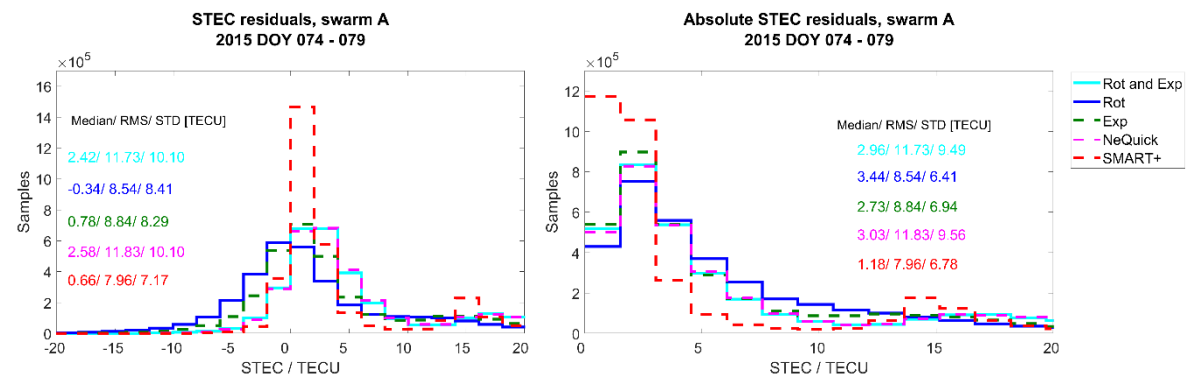


619

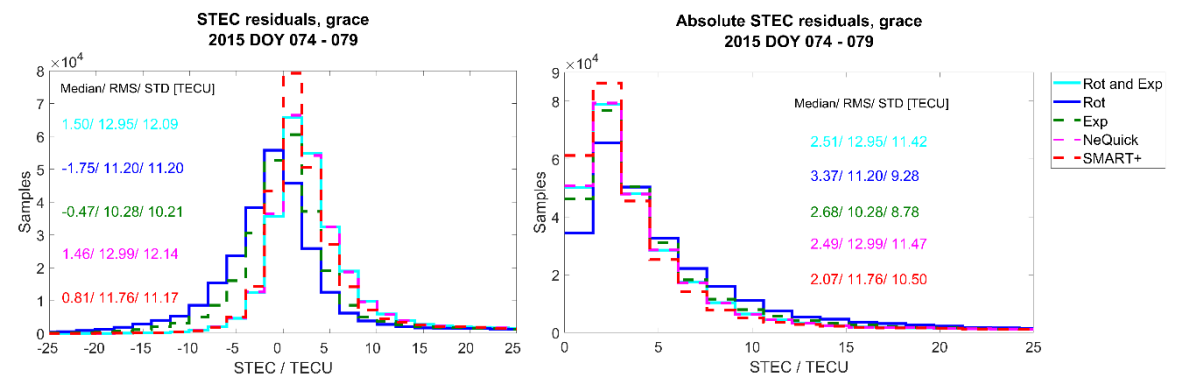
620 **Figure 13: Histograms of the STEC residuals (left) and absolute residuals (right) during the quiet period,**
 621 **for Swarm A.**



622
 623 **Figure 14: Histograms of the STEC residuals (left) and absolute residuals (right) during the quiet period,**
 624 **for GRACE.**

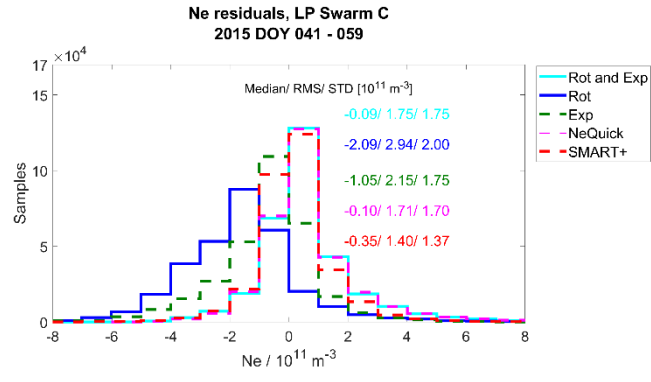
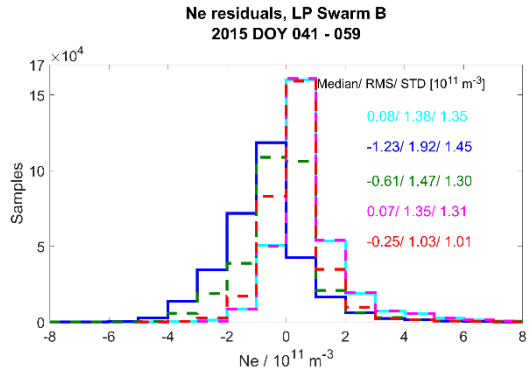
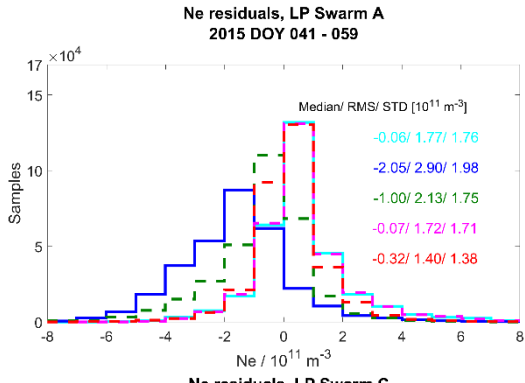


625
 626 **Figure 15: Histograms of the STEC residuals (left) and absolute residuals (right) during the perturbed**
 627 **period, for Swarm A.**



628
 629 **Figure 16: Histograms of the STEC residuals (left) and absolute residuals (right) during the perturbed**
 630 **period, for GRACE.**

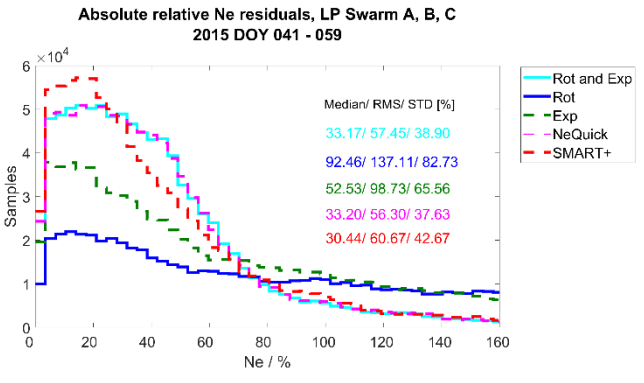
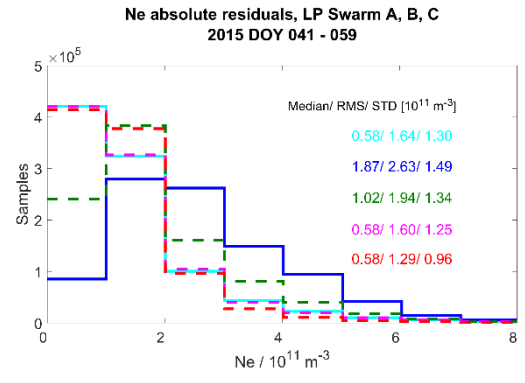




631

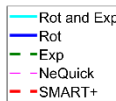
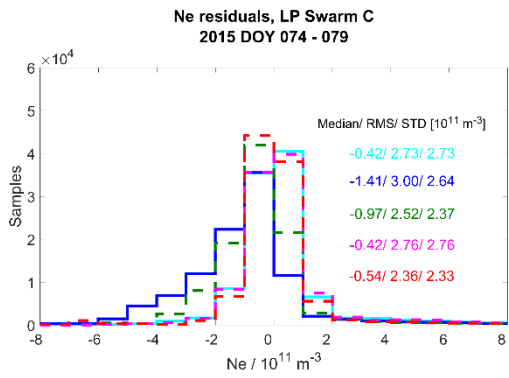
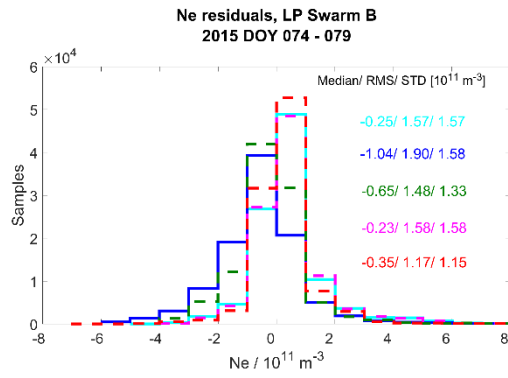
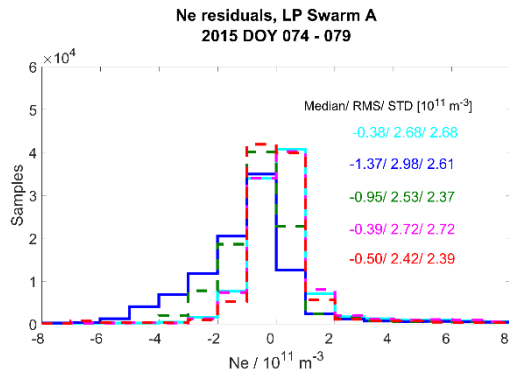
632

633 **Figure 17: Validation with LP data – distribution of the Swarm A, B, C (separated) electron density**
634 **residuals for the quiet period.**



635
636

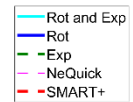
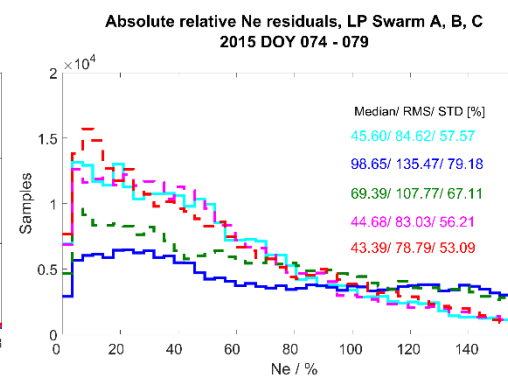
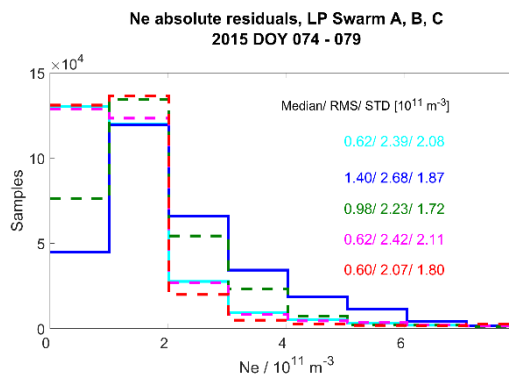
637 **Figure 18: Validation with LP data – distribution of the Swarm absolute and absolute relative electron**
638 **density residuals for the quiet period.**



639

640

641 **Figure 19: Validation with LP data – distribution of the Swarm A, B, C (separated) electron density**
642 **residuals for the perturbed period.**



643

644 **Figure 20: Validation with LP data – distribution of the Swarm absolute and absolute relative electron**
645 **density residuals for the perturbed period.**